Canted Eu magnetic structure in $EuMnSb_2$

Dongliang Gong,[1] Silu Huang,[1] Feng Ye,[2] Xin Gui,[3] Jiandi Zhang,[1] Weiwei Xie,[3] and Rongying Jin[1]
[1]*Department of Physics and Astronomy, Louisiana State University, Baton Rouge, Louisiana 70803, USA*
[2]*Neutron Scattering Division, Oak Ridge National Laboratory, Oak Ridge, Tennessee 37831, USA*
[3]*Department of Chemistry, Louisiana State University, Baton Rouge, Louisiana 70803, USA*

(Received 20 February 2020; revised manuscript received 28 May 2020; accepted 1 June 2020; published 15 June 2020)

Magnetic ordering breaks the time-reversal symmetry, greatly impacting material topological properties. We report the investigation of the magnetic properties of the layered $EuMnSb_2$, which has two sets of magnetic sublattices. Both the magnetization and electrical resistivity reveal two phase transitions with one at $T_{N,Eu} \sim 21$ K and the other at $T_{N,Mn} \sim 346$ K. Single crystal neutron diffraction refinement indicates that both transitions are originated from magnetic ordering. Below $T_{N,Mn}$, the Mn sublattice forms the *C*-type antiferromagnetic (AFM) structure with moments [$(4.5 \pm 0.6)\mu_B$ at 7 K] pointing along the *a* axis. Below $T_{N,Eu}$, the Eu sublattice forms the canted *A*-type AFM structure with moments [$(5.9 \pm 0.8)\mu_B$ at 7 K] lying in the *ac* plane but pointing $(41 \pm 1)^\circ$ away from the *a* axis. Quantitative analysis indicates that the spin-spin correlation length, while anisotropic, has long-range characteristic in all directions for both the Eu and Mn sublattices.

DOI: 10.1103/PhysRevB.101.224422

Layered manganese pnictides with the general formula $AMnPn_2$ (A = Ca, Sr, Ba, Eu or Yb, Pn = Sb or Bi) have attracted extensive attention, because of their intriguing topological electronic states that have an intimate relationship with magnetism [1–9]. Band structure calculations suggest that topological quasiparticles are hosted by conductive *Pn* zig-zag/square-net layers in $AMnPn_2$ [7,10–12]. Magnetism is from Mn and *A* ions (when *A* is magnetic) [1–14]. With accumulated investigations, it becomes clear that both crystal and magnetic structures play critical roles in the observed topological properties [7–14]. For example, the anisotropy of the Dirac cones in $(Sr/Ca)MnBi_2$ is strongly impacted by the local environment of the Bi layer [12,15]. It has also been observed that the magnetic structure and topological properties are affected by Sr and Mn concentrations in $Sr_{1-y}Mn_{1-z}Sb_2$ [14].

When *A* is magnetic, the physics of $AMnPn_2$ is even richer due to the interplay between *A* and Mn moments. For instance, the ordering of Eu moments significantly suppresses interlayer magnetic coupling in $EuMnBi_2$ [13]. Quantized Hall plateaus and profound Shubnikov–de Haas (SdH) oscillations are observed when Eu moments are canted [6,13,16,17]. This clearly demonstrates that a correct description of crystal and magnetic structures is essential for understanding material physics. Instead of the tetragonal structure like $EuMnBi_2$, $EuMnSb_2$ is found to form an orthorhombic structure (belonging to the *Pnma* space group) [18,19]. Recent powder neutron diffraction measurements suggest that the Eu sublattice forms the A-type antiferromagnetic (AFM) structure with spins along the *c* axis below 21 K, while the Mn sublattice exhibits the C-type AFM structure with spins along the *a* axis below ~350 K [19]. Disparities in both the crystal and magnetic structures of $EuMnBi_2$ and $EuMnSb_2$ call for further investigations of such a material family. In this article, we report our experimental investigations on $EuMnSb_2$ single crystals through magnetization, electrical resistivity, single crystal x-ray, and neutron diffraction measurements. We find that the Eu magnetic structure is different from the previous report obtained from powder neutron diffraction measurements [19]. Quantitative analysis of the spin-spin correlation of both Eu and Mn moments indicates three-dimensional (3D) magnetism, while the correlation length along the *a* direction is much shorter than that along the *bc* plane. Furthermore, the interaction between Eu and Mn moments is observed below 21 K.

Single crystals of $EuMnSb_2$ were synthesized in two steps. First, starting materials with Eu pieces (Alfa Aesar, 99.9%), Mn powder (Alfa Aesar, 99.9%), and Sb powder (Alfa Aesar, 99.9%) were mixed with a molar ratio of Eu : Mn : Sb = 1 : 1 : 2. The mixture was then placed in an alumina crucible and sealed into a fused silica tube after evacuation. The tube was heated up to 640 °C at a rate of 26 °C/h, and held at this temperature for 20 h. The furnace was then heated up to 840 °C at a rate of 2 °C/h and held at this temperature for 20 h, before quenched down to room temperature. Second, the mixture was regrounded and sealed in a quartz tube under vacuum for single-crystal growth in a floating-zone furnace. Single crystals were grown in a vacuum ($\sim 10^{-2}$ torr) with a growth speed of 0.5 mm/hr. As-grown single crystals have a typical size of $5 \times 5 \times 1\,mm^3$. The measurements below were carried out using as-grown single crystals from the same batch.

Magnetization measurements were performed using a Magnetic Property Measurement System (Quantum Design). The electrical resistivities were measured using the standard four-probe method in a Physical Property Measurement System (Quantum Design). Wavelength dispersive spectroscopy (WDS) was performed on a JOEL 8230 Electron Microprobe. Room temperature single crystal (as-grown) x-ray diffraction (XRD) measurements were carried out using a Panalytical

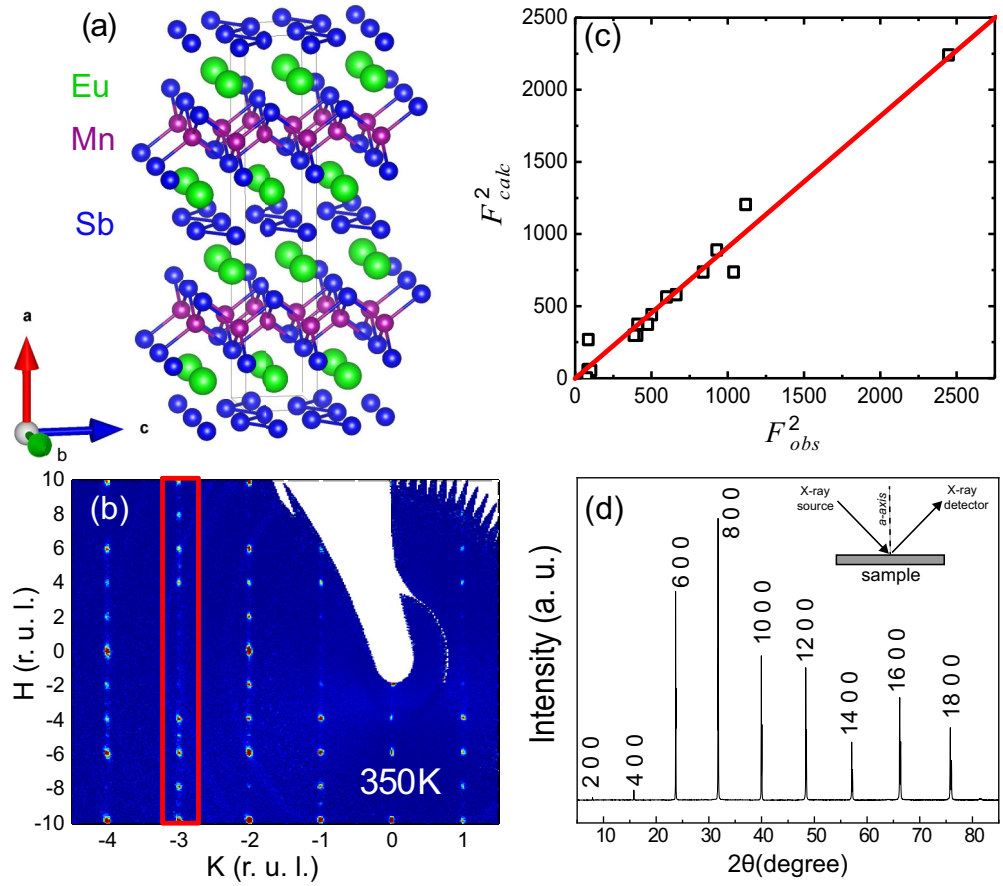

FIG. 1. (a) Crystalline structure of $EuMnSb_2$ with the *Pnma* space group. (b) Single crystal neutron diffraction in the (*H K* 2) plane at 350 K. Spots in the red box cannot exist in the tetragonal structure. (c) Calculated structure factor square versus the observed one. (d) XRD pattern obtained from an as-grown platelike single crystal at room temperature. Inset: schematic of x-ray beam with respect to the single crystal.

Empyrean multipurpose diffractometer with a wavelength of 1.5406 Å. Single crystal x-ray diffraction was also performed in a Bruker Apex II equipped with Mo radiation ($\lambda = 0.71073$ Å) at various temperatures from 300 to 100 K. Single crystals with a typical size $\sim 10\ \mu m \times 10\ \mu m \times 10\ \mu m$ were mounted on a Kapton loop and measurements were performed with an exposure time of 10 s per frame. Single crystal neutron diffraction experiments were carried out using the CORELLI instrument at the Spallation Neutron Source at Oak Ridge National Laboratory [20]. A single crystal with a mass of 47 mg ($9 \times 3 \times 0.5\,mm^3$) was attached to an aluminum plate in a manner to facilitate the inspection of the *HK*0 scattering plane. An extensive survey in the reciprocal space was performed at three temperatures (7, 150, and 350 K). At each temperature, the sample was rotated with a step of 2° over the range of 180°. Data reduction and analysis were conducted using MANTID software [21]. Magnetic structures were analyzed with SARAH software [22]. All refinements were performed with FULLPROF software [23].

Figure 1(a) shows the crystal structure of $EuMnSb_2$, which consists of Eu, $MnSb_4$, Eu, Sb layers alternately stacking along the *a* axis. This is based on the neutron diffraction data at 350 K as shown in Fig. 1(b). Spots in the red box are not expected if the structure of $EuMnSb_2$ were tetragonal. The refinement indicates that $EuMnSb_2$ crystallizes in an orthorhombic structure (space group *Pnma*) with the lattice constants $a = 22.56(7)$ Å, $b = 4.37(1)$ Å, and $c = 4.41(1)$ Å at 350 K. As can be seen in Fig. 1(c), the calculated structure factor square (F^2_{calc}) matches well with the observed structure factor square (F^2_{obs}), indicating excellent structure refinement. While both the crystal structure and lattice parameters are consistent with that reported in Ref. [18], WDS measurements on one of our crystals give the actual Eu : Mn : Sb = 1 : 1.1 : 2, which is obtained by averaging measurements at ten different locations. The standard deviation is ±2% for each element. At present, it is unclear how extra Mn affects the structure and physical properties. According to previous report on $Sr_{1-y}Mn_{1-z}Sb_2$ [14], Mn deficiency results in reduced Mn moment. The orthorhombic structure of $EuMnSb_2$ requires the zig-zag arrangement of Sb atoms in the Sb layer, instead of the square Bi network in tetragonal $EuMnBi_2$ [6,13]. Figure 1(d) shows the XRD pattern obtained from an as-grown platelike single crystal. All peaks are extremely sharp and can be indexed with the *Pnma* structure. This indicates the high quality of our single crystals without obvious stacking faults along the *a* direction.

Figure 2(a) shows the temperature dependence of the magnetic susceptibilities (χ_a and χ_{bc}) measured under the magnetic field $H = 1T$. Note that there is almost no anisotropy at high temperatures until reaching $T < T_{N,Eu} = 21$ K, the AFM

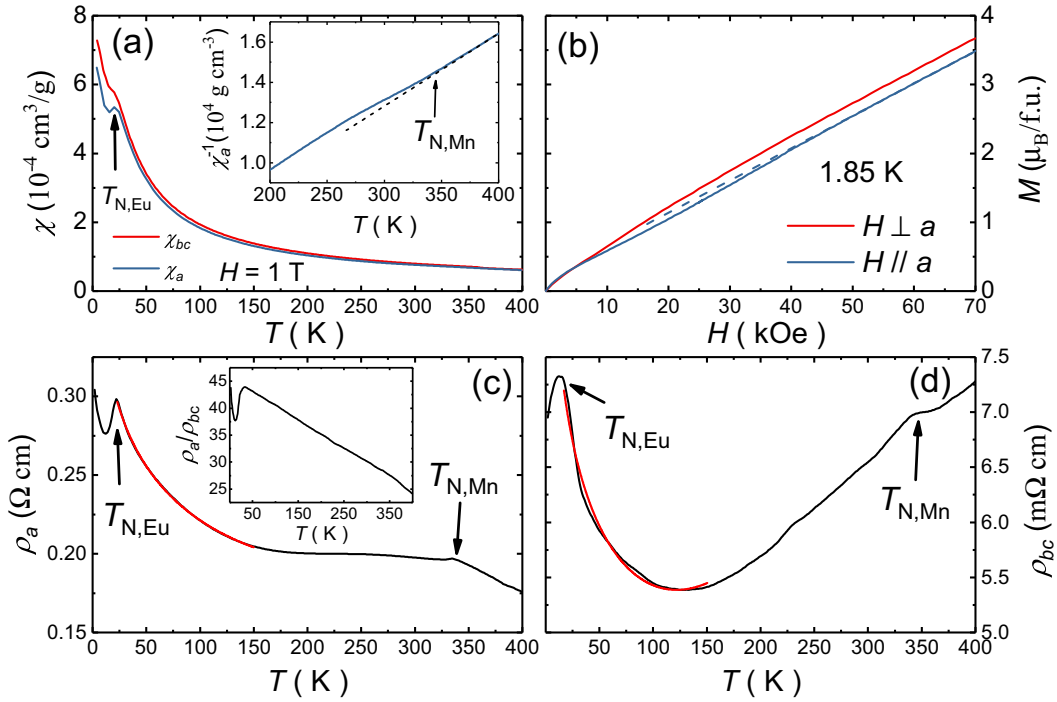

FIG. 2. (a) Temperature dependence of the magnetic susceptibilities (χ_a and χ_{bc}) measured under 1 T. Inset: χ_a^{-1}(T) with a dashed line representing the high-temperature behavior (see text). (b) Magnetic field dependence of the magnetization at 1.85 K. The dashed line is the linear extrapolation of M(H) from high field. (c) Temperature dependence of the electrical resistivity ρ_a with indication of $T_{N,Mn}$ and $T_{N,Eu}$. The red curve is the fit of ρ_a to $A + B\ln(T_{SF}/T)$ (see text). Inset: temperature dependence of the resistivity anisotropy ρ_a/ρ_{bc}. (d) Temperature dependence of the electrical resistivity ρ_{bc} with indication of $T_{N,Mn}$ and $T_{N,Eu}$. The red curve is the fit of ρ_{bc} to $A + B\ln(T_{SF}/T)$ (see text).

ordering temperature of Eu moments according to a previous report [18]. Below $T_{N,Eu}$, both χ_a and χ_{bc} reveal a peak before a further upturn. While it is not obvious, χ_a deviates from the high-temperature Curie-Weiss behavior (represented by the dashed line) below $T_{N,Mn} = 346$ K as illustrated in the inset of Fig. 2(a). Surprisingly, the field dependence of the magnetization (M) taken at $T = 1.85$ K shows the absence of metamagnetic transition in M_a, while both M_a and M_{bc} are not strictly linear dependent on H as shown in Fig. 2(b). This is different from that reported in Ref. [18], which shows a spin-flop transition around 15 kOe at 2 K in M_a.

With the layered crystal structure, the almost isotropic magnetic susceptibility of $EuMnSb_2$ is surprising. To understand the structure-property relationship, we further investigate the resistivity anisotropy, ρ_a and ρ_{bc}, which are displayed in Figs. 2(c) and 2(d), respectively. First of all, there is obvious resistivity anisotropy in both quantity and temperature dependence. Note $\rho_a \gg \rho_{bc}$, consistent with the layered structure shown in Fig. 1(a). At 400 K, $\rho_a/\rho_{bc} \sim 25$, which increases with decreasing temperature as shown in the inset of Fig. 2(c). At $T_{N,Mn}$, the resistivity response is much more obvious than the susceptibility. Below $T_{N,Mn}$, the increase of ρ_a is much slower than that at high temperatures, indicating the suppression of spin-charge scattering. On the other hand, ρ_{bc} exhibits a small kink at $T_{N,Mn}$, then continues to decrease with temperature. Such a resistivity response is consistent with the C-type AFM ordering of Mn moments [19]. The AFM configuration of Mn moments in the bc plane increases spin scattering, while the ferromagnetic (FM) configuration of Mn along the a axis reduces spin scattering. At $T_{N,Eu}$, ρ_a and ρ_{bc} decrease, which are difficult to explain with the A-type AFM configuration of Eu proposed in Ref. [19]. Overall, both ρ_a and ρ_{bc} show upturn between $T_{N,Eu}$ and ~150 K, which are likely due to interaction between charge carriers and fluctuating Eu moments. According to early studies [24,25], the electrical resistivity due to spin fluctuation (SF) can be described by $\rho = A + B\ln(T_{SF}/T)$, where A and B are constants and T_{SF} is the onset temperature of SF. Using this formula, we fit both ρ_a and ρ_{bc} between 25 and 150 K. As shown in Figs. 2(c) and 2(d), the formula fits our experimental data very well (red curves) with $A_a = 0.193\ \Omega$ cm, $B_a = 49.2$ mΩ cm, and $T_{SF\text{-}a} = 180.6$ K for ρ_a, and $A_{bc} = 5.4$ mΩ cm, $B_{bc} = 0.8$ mΩ cm, and $T_{SF\text{-}bc} = 113.3$ K for ρ_{bc}. Compared to $T_{SF\text{-}a}$, $T_{SF\text{-}bc}$ is smaller, which should be attributed to metallic contribution in the bc plane, which is not taken into account in the fitting [see Fig. 2(d)]. Nevertheless, the fitting result indicates that the fluctuating moment of Eu impacts physical properties in a wide temperature range even though it orders at a much lower temperature (21 K). This also explains why the thermally activated resistivity model fails to describe the resistivity below 100 K in Ref. [18].

As having difficulty to explain the resistivity drop below $T_{N,Eu}$, we examine the magnetic structure of $EuMnSb_2$ through single crystal neutron diffraction. In the measured temperature range (between 7 and 350 K), there is no sign for obvious change of the lattice structure, consistent with previously reported results [18,19]. The crystal structure remains orthorhombic with the *Pnma* space group, which is also served to index all the diffraction peaks in this article. Figures 3(a), 3(c), and 3(e) show the (H K 0) plane contour

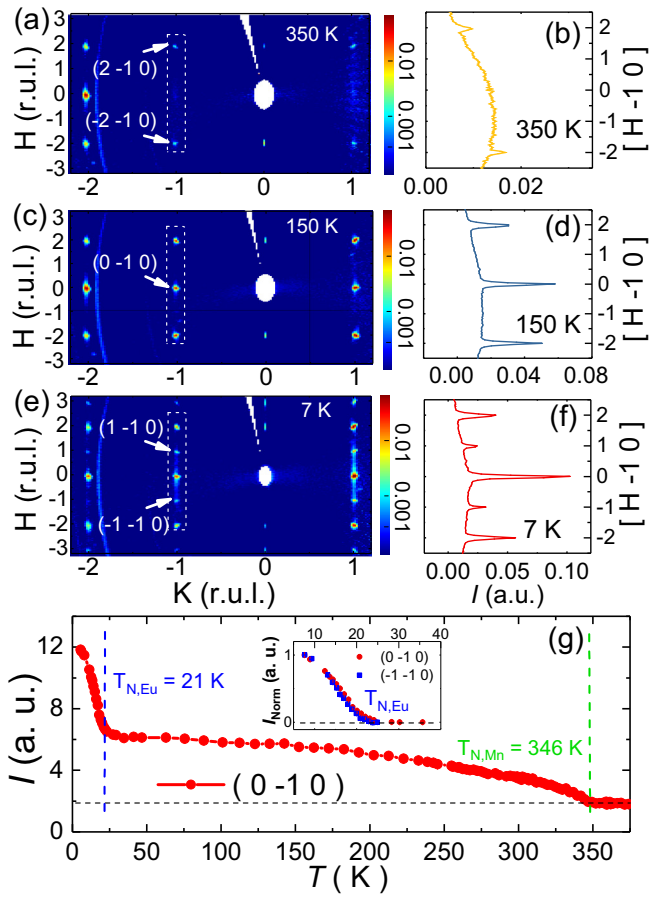

FIG. 3. (a)–(f) Contour map of neutron intensity of $EuMnSb_2$ in the (H K 0) plane and the intensity profile for the area indicated by the dashed rectangular box at 350 K (a), (b), 150 K (c), (d), and 7 K (e), (f), respectively. (g) Temperature dependence of the magnetic peak (0 −1 0) intensity. Inset: temperature dependence of the magnetic peak counts at (0 −1 0) and (−1 −1 0) below 40 K normalized via $I_{\mathrm{Norm}} = (I–I_{25\,\mathrm{K}})/(I_{7\,\mathrm{K}} - I_{25\,\mathrm{K}})$.

maps of neutron diffraction intensity for $EuMnSb_2$ at 350, 150, and 7 K, respectively. At 350 K, the diffraction peaks result completely from nuclear diffraction expected from the *Pnma* crystal structure. Compared to that at 350 K, a new peak, (0 −1 0), emerges at 150 K and 7 K. Additional peaks including (1 −1 0) and (−1 −1 0) can be seen at 7 K as indicated in the dashed rectangular box in Fig. 3(e). These new peaks are forbidden in the *Pnma* space group, thus can be attributed to magnetic scattering. As can be seen in Figs. 3(b), 3(d), and 3(f), the magnetic peak (0 −1 0) does not appear at 350 K, but emerges upon decreasing temperature. Figure 3(g) shows the temperature dependence of the integrated intensity of the magnetic diffraction peak (0 −1 0). The peak intensity becomes finite below $T_{\mathrm{N,Mn}} = 346\,\mathrm{K}$, and increases with decreasing temperature. It is more or less saturated below 75 K, until a sharp rise at $T_{\mathrm{N,Eu}} = 21\,\mathrm{K}$. This confirms that two phase transitions at $T_{\mathrm{N,Mn}}$ and $T_{\mathrm{N,Eu}}$ are due to the magnetic ordering of the Mn and Eu moments, respectively. While the (−1 −1 0) and (1 −1 0) peaks appear only below $T_{\mathrm{N,Eu}}$, the temperature dependence of their normalized intensities, which are obtained via $I_{\mathrm{Norm}} = (I - I_{25\,\mathrm{K}})/(I_{7\,\mathrm{K}} - I_{25\,\mathrm{K}})$, is the same as that of the (0 −1 0) peak as can be seen in the inset of Fig. 3(g). These intensities are served as the order parameters of magnetic phase transitions in the system.

TABLE I. Representational analysis for the magnetic structure of $EuMnSb_2$. Here, a, b, and c indicate the spin orientation, A, C, and G represent three types of AFM, and F denotes the ferromagnetic state.

Irrep	Orientation	Mn	Eu
Γ1	*b*	G	
Γ2	*a*	C	A
	c	A	
Γ3	*a*	F	F
	c	G	
Γ4	*b*	A	
Γ5	*b*	F	F
Γ6	*a*	A	
	c	C	A
Γ7	*a*	G	
	c	F	F
Γ8	*b*	C	A

We now describe the magnetic structure refinement. First of all, all magnetic diffraction peaks appear at the integer indices implying a commensurate configuration with the magnetic propagation wave vector $\mathbf{k} = (0, 0, 0)$ Using the SARAH software, we identify eight possible irreducible representations (Γ1, Γ2, Γ3, Γ4, Γ5, Γ6, Γ7, Γ8), as shown in Table I, suitable for the Mn sublattice. The irreducible representations Γ1, Γ4, Γ5, Γ8 are 1D with spins along the *b* direction, whereas Γ2, Γ3, Γ6, Γ7 are 2D with spins along the *a* and *c* directions. The observed (0 −1 0) magnetic diffraction peak cannot be reproduced with the Γ1, Γ3, Γ4, Γ5, Γ7, and Γ8 representations. Thus, there are only Γ2 and Γ6 representations that can describe the (0 −1 0) magnetic peak. However, due to the weak orthorhombicity of the crystal structure with $b \sim c$, our $EuMnSb_2$ sample is twinned, which is also observed in isostructural $Sr_{1-y}Mn_{1-z}Sb_2$ [14]. In this case, the observed (0 −1 0) diffraction is equivalent to the (0 0 1) peak from the twinned domain, which is allowed in the Γ1, Γ7, and Γ8 representations. On the other hand, the Γ1 and Γ7 representations would also produce (1 −1 0) and (−1 −1 0) diffraction peaks, which are even stronger than the (0 −1 0) peak. Γ1 and Γ7 representations can be excluded, due to the absence of the (1 −1 0) and (−1 −1 0) peaks at $T_{N,\mathrm{Eu}} < T < T_{N,\mathrm{Mn}}$. After subtracting the nuclear contribution taken at 350 K, we selected eight magnetic diffraction peaks for Mn magnetic structure refinement using the Γ2, Γ6, and Γ8 representations. The R factors are 7.18, 15.99, and 16.08 for Γ2, Γ6, Γ8, respectively. This indicates that the Γ2 representation gives the best refinement to our data. The Mn magnetic structure corresponding to the Γ2 representation is displayed in Fig. 4, showing that all Mn moments are along the *a* direction, with the checkboard AFM in the *bc* plane. This confirms the *C*-type AFM structure of Mn as obtained from powder neutron diffraction [19]. The refined magnetic moment of Mn is $(4.0 \pm 0.1)\mu_{\mathrm{B}}$ at 150 K, smaller than the expected value for Mn^{2+} ($5\mu_B$).

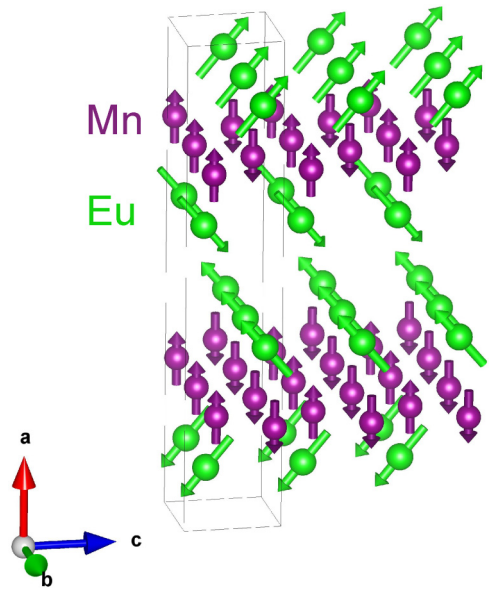

FIG. 4. Magnetic structure of Eu sublattice and Mn sublattice. The Mn ordering forms the C-type AFM structure below 346 K with the moments along the *a* axis. The Eu ordering forms a canted A-type AFM structure below 21 K with spins lying in the *ac* plane but 41° away from the *a* axis without changing the Mn magnetic structure.

Below $T_{N,Eu}$, a significant increase in the intensity of (0 −1, 0) and new magnetic diffraction peaks at (1 −1 0) and (−1 −1 0) are observed, indicating new magnetic ordering due to the Eu sublattice. Based on the crystal structure, the Eu sublattice allows having the same possible irreducible representations (Γ1, Γ2, Γ3, Γ4, Γ5, Γ6, Γ7, Γ8) as the Mn sublattice, since they have the same Wyckoff site and magnetic propagation vector (Table I). For the same sake of argument as for the Mn sublattice, the Γ1, Γ3, Γ4, Γ5, and Γ7 magnetic representations can be excluded here. Furthermore, the Γ6 and Γ8 representations can be excluded, since they do not allow us to have the observed (3 0 0) and (-3 0 0) diffraction peaks. Hence, the only allowed representation is Γ2 for the Eu sublattice. We selected 11 magnetic diffraction peaks for the magnetic structure refinement with Γ2 (Mn) + Γ2 (Eu) representations below $T_{N,Eu}$. At 7 K, the refined moment of Eu^{2+} is $(4.4 \pm 0.8)\mu_B$ along the *a* axis and $(3.8 \pm 0.9)\mu_B$ along the *c* axis, so that the spins of Eu are aligned in the *ac* plane. The moment of Mn^{2+} reaches $(4.5 \pm 0.6)\mu_B$ at 7 K from $(4.0 \pm 0.1)\mu_B$ at 150 K. Similar to Mn, the ordered moment of Eu $[(5.9 \pm 0.8)\mu_B]$ is also smaller than the expected value $(7\mu_B)$. It should be mentioned that, for the above magnetic structure refinement, absorption correction was made to the intensities of the selected 11 peaks, as Eu has a large neutron absorption cross section. Such a correction takes into account the neutron attenuation and neutron traveling path. As a result, the obtained Mn moment for $EuMnSb_2$ is similar to that for $SrMnSb_2$ $(4.0\mu_B$ at 80 K) [9,14].

The refined magnetic structure of $EuMnSb_2$ is shown in Fig. 4. The Mn sublattice forms the *C*-type AFM structure below $T_{N,Mn} = 346$ K, whereas the Eu sublattice forms the canted *A*-type AFM structure with the Eu moments about 41° away from the *a* axis within the *ac* plane below $T_{N,Eu} \sim 21$ K. While the former is consistent with previous power neutron diffraction result [19], the latter differs significantly. This is mainly due to the absence of the (1 −1 0) and (−1 −1 0) peaks in powder neutron diffraction, leading to the conclusion of zero Eu moment along the *a* axis [19]. At present, the origin of such a discrepancy is unknown. Given the crystal structure and lattice parameters, single crystals grown by the floating-zone method show no difference with that prepared by the Sn flux method [18]. Whether the inclusion of Sn results in the different magnetic structure of Eu requires further investigation.

With the establishment of two magnetic structures corresponding to Mn and Eu spin ordering, we would like to elucidate the nature of each magnetic order and the interplay between Mn and Eu sublattice. Figure 5(a) shows the intensity of the (0 −1 0) peak as a function of the reduced temperature $t = (T_{N,Mn} - T)/T_{N,Mn}$ near $T_{N,Mn}$. The linear relationship in the double logarithmic plot allows us to extract the critical exponent β_{Mn} for Mn ordering transition [26]. As can be seen in Fig. 5(a), data can be well fitted with $\beta_{Mn} = 0.25 \pm 0.01$, which is much higher than that for the 2D ($\beta \sim 0.125$) but lower than that for the 3D ($\beta \sim 0.327$) case in the Ising model [27]. The low β_{Mn} is not surprising given the spacing between adjacent Mn along the *a* axis is 10 Å. In Fig. 5(b), the same linear fitting is applied to the (−1 −1 0) peak intensity, which is the sole contribution of Eu moment. The obtained critical exponent $\beta_{Eu} = 0.35 \pm 0.01$, indicating 3D ordering [27]. In view of the crystal structure [Fig. 1(a)], the distance between adjacent Eu layers is roughly half of that of the Mn layers. Thus, the Eu magnetic interaction has a 3D character. Note that the resistivity anisotropy [see the inset of Fig. 2(c)] also drops below $T_{N,Eu}$, consistent with the 3D magnetic ordering of Eu moment.

The spin-spin correlation length ξ can further characterize the effective dimensionality of magnetic ordering. For obtaining such information, we construct a diffraction intensity profile along a particular direction (Q) (i.e., H, K, or L direction) by integrating intensity over a square area with a width of −0.15 to +0.15 (r.u.l) normal to the Q direction. For example, the profile along the (H, −1, 0) direction (i.e., H cut) is obtained by the integration of intensity over a square area centered at (H −1 0) with $\Delta K(\Delta L)$ from −0.15 (r.u.l) to +0.15. Figure 5(c) shows the H cut around the (H −1 0) peak at 150 K, which only contains the contribution from Mn ordering. Note the H-cut intensity profile exhibits a broad Lorentzian profile (red curve). The correlation length calculated after the instrumental resolution correction is $x_{Mn} \sim 124 \pm 3$ Å at 150 K, which is about five times of the *a*-axis lattice constant (22.5 Å). On the other hand, the K-cut intensity profile exhibits a narrower peak with a Gaussian characteristic (blue curve) close to the instrumental resolution limit, indicating long-range magnetic ordering in the *b* axis. The lower limit of the spin-spin correlation length is about 230 Å, which is estimated with the instrumental resolution. The L-cut intensity profile also indicates a long-range order along the *c* axis (not shown here). The analysis of spin-spin correlation indicates that Mn magnetic interaction is 3D but anisotropic.

The same analysis is applied for the Eu sublattice. Figure 5(d) shows the intensity profile around the (−1 −1 0)

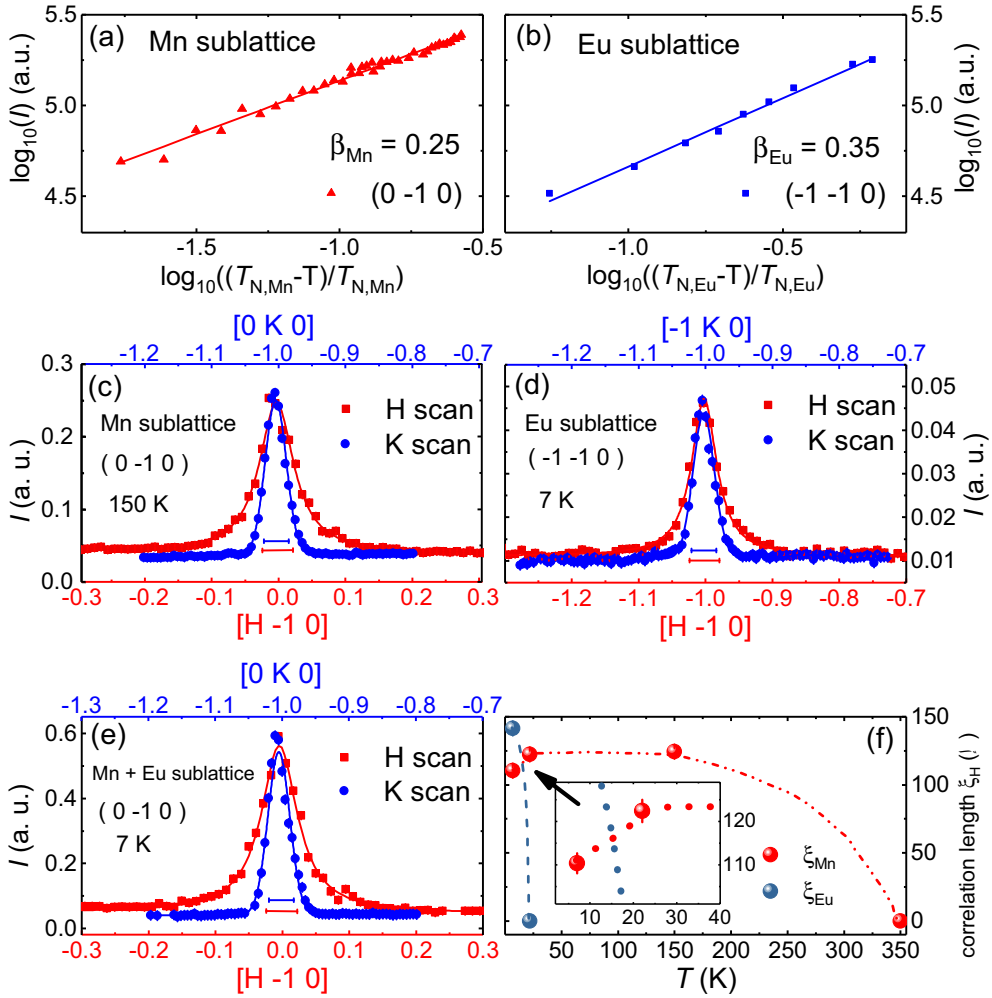

FIG. 5. (a) Intensity at (0 −1 0) versus $((T_{N,Mn} - T)/T_{N,Mn})$ plotted in the double logarithmic scales. (b) Intensity at (−1 −1 0) versus $((T_{N,Eu} - T)/T_{N,Eu})$ plotted in the double logarithmic scales. (c) *H* and *K* scans around (0 −1 0) at 150 K. (d) *H* and *K* scans around (−1 −1 0) at 7 K. (e) *H* and *K* scans around (0 −1 0) at 7 K. (f) Temperature dependence of the spin-spin correlation length along the *H* direction at (0 −1 0) (red) and (−1 −1 0) (blue), respectively. Inset: enlarged low-temperature behavior.

peak at 7 K, which only contains the contribution from Eu magnetic ordering. While the *H* cut shows a broad Lorentzian profile, the *K* cut exhibits a Gaussian-like profile, reflecting shorter spin-spin correlation along the *a* axis but longer along the *b* axis. The correlation length along the *a* axis is $\xi_{Eu} \sim 141 \pm 5$ Å, reaching ∼30 Eu layers. Anisotropic 3D Eu ordering is consistent with the large critical exponent $\beta_{Eu} \sim 0.35$ [Fig. 5(b)]. For both Mn and Eu, $\xi_a < \xi_{bc}$, likely due to the layered structure of $EuMnSb_2$.

We check the full width at half maximum (FWHM) of the (0 −1 0) peak at 7 K. Figure 5(e) shows the ***Q*** cut around the (0 −1 0) peak at 7 K, which contains the contribution from both Eu and Mn ordering. The *K* cut still shows the Gaussian-like profile, indicating a long-range order along the *b* axis. The *H* cut shows the Lorentzian profile, which is broader than that at $T > T_{N,Eu}$. The spin-spin correlation length extracted from the FWHM, after taking into account of the instrumental resolution, is about 109 ± 3 Å at 7 K. Figure 5(f) shows the temperature dependence of the spin-spin correlation length ξ along the *H* direction, clearly demonstrating the reduced correlation length of Mn in the *a* axis below $T_{N,Eu}$, as highlighted in the inset. This can be understood by considering the different magnetic structure of Eu ordering from Mn, resulting in the destructive magnetic interaction.

Since there are interactions between the Mn and Eu sublattices at low temperatures, one should consider the possible change of the Mn magnetic structure due to Eu ordering. Assuming that the Mn magnetic structure changes from the Γ2 to Γ6 representation after Eu ordering, one may then expect the low-temperature magnetic structure represented by Γ6 (Mn) + Γ2 (Eu). Although the refinement can also be converged with the twinning ratio of 0.8 : 0.2 between two sets of domains in the *bc* plane (Fig. 1(d) shows no sign of additional contribution from the *b* and *c* directions), the result is unrealistic as the actual twinning ratio should be nearly 0.52 : 0.48, based on nuclear diffraction intensity ratio of (0 2 0) and (0 0 2) peaks [28] (see Fig. S1). Another possibility would be that the Mn magnetic structure changes from the Γ2 to Γ8 representation below $T_{N,Eu}$ as discussed above. However, this scenario can be also excluded, since the (0 −1 0) peak exists with enhanced intensity when the temperature is lower than $T_{N,Eu}$ [28] (see Fig. S2), which is forbidden for

the Γ8 representation. Therefore, our results suggest that the interaction between the Mn and Eu sublattices is too weak to change the Mn magnetic structure below $T_{N,Eu}$.

According to theoretical calculations, a slight canting of Mn moments can facilitate the formation of the Weyl band structure [10]. The robust *C*-type Mn magnetic structure in $EuMnSb_2$ seems unfavorable for the topological band structure. On the other hand, in isostructural $Sr_{1-y}Mn_{1-z}Sb_2$, the canted Mn magnetic structure is observed, accompanied by the nearly massless relativistic fermions [14,29]. It requires further investigation to see if Mn deficiency can modify the Mn magnetic structure in this system. In $EuMnBi_2$, the Eu moments are collinearly aligned with the Mn moments at zero magnetic field [13]. By applying the magnetic field, the Eu moments change to the canted structure [13]. Our result shows that the Eu moments are already canted at zero magnetic field in $EuMnSb_2$. Further experimental and theoretical investigations are necessary to understand its impact on the topological properties.

In conclusion, we have investigated the crystal structure, electrical, and magnetic properties of $EuMnSb_2$ single crystals. Both single crystal x-ray and neutron diffraction confirm its orthorhombic structure belonging to the *Pnma* space group. The magnetization and electrical resistivity reveal two phase transitions at $T_{N,Eu} = 21$ K and $T_{N,Mn} = 346$ K. Single crystal neutron diffraction refinement indicates that the Mn sublattice orders in the *C*-type AFM structure with moments pointing to the *a* axis below 346 K, and the ordered moment is $(4.5 \pm 0.6)\mu_B$ at 7 K. The Eu sublattice orders in the canted *A*-type AFM structure with an angle of $(41 \pm 1)^\circ$ from the *a* axis at 7 K. The Eu total ordered moment is $(5.9 \pm 0.8)\mu_B$, with $(4.4 \pm 0.8)\mu_B$ along the *a* axis and $(3.8 \pm 0.9)\mu_B$ along the *c* axis. For both the Mn and Eu sublattices, we obtain that the spin-spin correlation length along the *a* axis is much shorter than that along the *b* and *c* axes, indicating anisotropic magnetic coupling. The interaction between these two sublattices enhances the complexity of the system.

We thank Y. Li and L. Xing for fruitful discussion, and M. Pan for proofreading. This material is based upon work supported by the US Department of Energy under EPSCoR Grant No. DE-SC0012432 with additional support from the Louisiana Board of Regents. This research used resources at the Spallation Neutron Source and the High Flux Isotope Reactor, which are DOE Office of Science User Facilities operated by the Oak Ridge National Laboratory.

[1] N. P. Armitage, E. J. Mele, and A. Vishwanath, Rev. Mod. Phys. **90**, 015001 (2018).
[2] P. Tang, Q. Zhou, G. Xu, and S.-C. Zhang, Nat. Phys. **12**, 1100 (2016).
[3] J. K. Wang, L. L. Zhao, Q. Yin, G. Kotliar, M. S. Kim, M. C. Aronson, and E. Morosan, Phys. Rev. B **84**, 064428 (2011).
[4] K. Wang, D. Graf, L. Wang, H. Lei, S. W. Tozer, and C. Petrovic, Phys. Rev. B **85**, 041101(R) (2012).
[5] L. Li, K. Wang, D. Graf, L. Wang, A. Wang, and C. Petrovic, Phys. Rev. B **93**, 115141 (2016).
[6] A. F. May, M. A. McGuire, and B. C. Sales, Phys. Rev. B **90**, 075109 (2014).
[7] M. A. Farhan, G. Lee, and J. H. Shim, J. Phys.: Condens. Matter **26**, 042201 (2014).
[8] A. Wang, I. Zaliznyak, W. Ren, L. Wu, D. Graf, V. O. Garlea, J. B. Warren, E. Bozin, Y. Zhu, and C. Petrovic, Phys. Rev. B **94**, 165161 (2016).
[9] Y. Liu, T. Ma, L. Zhou, W. E. Straszheim, F. Islam, B. A. Jensen, W. Tian, T. Heitmann, R. A. Rosenberg, J. M. Wilde, B. Li, A. Kreyssig, A. I. Goldman, B. G. Ueland, R. J. McQueeney, and D. Vaknin, Phys. Rev. B **99**, 054435 (2019).
[10] S. Borisenko, D. Evtushinsky, Q. Gibson, A. Yaresko, K. Koepernik, T. Kim, M. Ali, J. van den Brink, M. Hoesch, A. Fedorov, E. Haubold, Y. Kushnirenko, I. Soldatov, R. Schäfer, and R. J. Cava, Nat. Commun. **10**, 3424 (2019).
[11] S. Huang, J. Kim, W. Shelton, E. Plummer, and R. Jin, Proc. Natl. Acad. Sci. USA **114**, 6256 (2017).
[12] G. Lee, M. A. Farhan, J. S. Kim, and J. H. Shim, Phys. Rev. B **87**, 245104 (2013).
[13] H. Masuda, H. Sakai, M. Tokunaga, Y. Yamasaki, A. Miyake, J. Shiogai, S. Nakamura, S. Awaji, A. Tsukazaki, H. Nakao, Y. Murakami, T.-h. Arima, Y. Tokura, and S. Ishiwata, Sci. Adv. **2**, e1501117 (2016).
[14] J. Liu, J. Hu, Q. Zhang, D. Graf, H. B. Cao, S. Radmanesh, D. Adams, Y. Zhu, G. Cheng, X. Liu, W. A. Phelan, J. Wei, M. Jaime, F. Balakirev, D. A. Tennant, J. F. DiTusa, I. Chiorescu, L. Spinu, and Z. Q. Mao, Nat. Mater. **16**, 905 (2017).
[15] Y. Feng, Z. Wang, C. Chen, Y. Shi, Z. Xie, H. Yi, A. Liang, S. He, J. He, Y. Peng, X. Liu, Y. Liu, L. Zhao, G. Liu, X. Dong, J. Zhang, C. Chen, Z. Xu, X. Dai, Z. Fang, and X. J. Zhou, Sci. Rep. **4**, 5385 (2014).
[16] H. Masuda, H. Sakai, M. Tokunaga, M. Ochi, H. Takahashi, K. Akiba, A. Miyake, K. Kuroki, Y. Tokura, and S. Ishiwata, Phys. Rev. B **98**, 161108(R) (2018).
[17] Y. Iwasaki and T. Morinari, J. Phys. Soc. Jpn. **87**, 033706 (2018).
[18] C. Yi, S. Yang, M. Yang, L. Wang, Y. Matsushita, S. Miao, Y. Jiao, J. Cheng, Y. Li, K. Yamaura, Y. Shi, and J. Luo, Phys. Rev. B **96**, 205103 (2017).
[19] J.-R. Soh, P. Manuel, N. M. B. Schröter, C. J. Yi, F. Orlandi, Y. G. Shi, D. Prabhakaran, and A. T Boothroyd, Phys. Rev. B **100**, 174406 (2019).
[20] F. Ye, Y. Liu, R. Whitfield, R. Osborn, and S. Rosenkranz, J. Appl. Crystallogr. **51**, 315 (2018).
[21] T. M. Michels-Clark, A. T. Savici, V. E. Lynch, X. Wang, and C. M. Hoffmann, J. Appl. Crystallogr. **49**, 497 (2016).
[22] A. Wills, Physica B **276–277**, 680 (2000).
[23] J. Rodríguez-Carvajal, Physica B **192**, 55 (1993).
[24] N. Rivier and V. Zlatic, J. Phys. F **2**, L99 (1972).
[25] Z. Altounian, S. V. Dantu, and M. Dikeakos, Phys. Rev. B **49**, 8621 (1994).
[26] F. Ye, L. Zhou, S. Larochelle, L. Lu, D. P. Belanger, M. Greven, and D. Lederman, Phys. Rev. Lett. **89**, 157202 (2002).
[27] A. Pelissetto and E. Vicari, Phys. Rep. **368**, 549 (2002).
[28] See Supplemental Material at http://link.aps.org/supplemental/10.1103/PhysRevB.101.224422 for details of twining ratio and representational analysis.
[29] Q. Zhang, S. Okamoto, M. B. Stone, J. Liu, Y. Zhu, J. DiTusa, Z. Mao, and D. A. Tennant, Phys. Rev. B **100**, 205105 (2019).